Interaction of barn owl leading edge serrations with freestream turbulence

Alden Midmer[1], Christoph Brücker[1], Matthias Weger[2]
Hermann Wagner[2], Horst Bleckmann[3]

[1] *City, University of London, Northampton Square 10, EC1V0HB London, UK*

[2] *Institute of Biology II, RWTH Aachen University, Aachen, Germany*

[3] *Institute of Zoology, Rheinische Friedrich-Wilhelms Universität Bonn, Bonn, Germany*

Corresponding author: Alden Midmer Email: alden.midmer@city.ac.uk

Abstract

The silent flight of barn owls is associated with wing and feather specialisations. Three special features are known: a serrated leading edge that is formed by free-standing barb tips which appears as a comb-like structure, a soft dorsal surface, and a fringed trailing edge. We used a model of the leading edge comb with 3D-curved serrations that was designed based on 3D micro-scans of rows of barbs from selected barn-owl feathers. The interaction of the flow with the serrations was measured with Particle-Image-Velocimetry in a flow channel at uniform steady inflow and was compared to the situation of inflow with freestream turbulence, generated from the turbulent wake of a cylinder placed upstream. In steady uniform flow, the serrations caused regular velocity streaks and a flow turning effect. When vortices of different size impacted the serrations, the serrations reduced the flow fluctuations downstream in each case, exemplified by a decreased root-mean-square value of the fluctuations in the wake of the serrations. This attenuation effect was stronger for the spanwise velocity component, leading to an overall flow homogenization. Our findings suggest that the serrations of the barn owl provide a passive flow control leading to reduced leading-edge noise when flying in turbulent environments.

Symbols and abbreviations

Symbol	Units	Description
D	mm	Cylinder diameter
f	Hz	Shedding frequency
H	mm	Serration height
L	mm	Serration length
PIV	-	Particle image velocimetry
P_L	mm	Plate length
Ma	-	Mach number
Re_b	-	Barb, height Reynolds number
Re_c	-	Chord Reynolds number
RMS	-	Root mean square
SD	-	Standard deviation
St	-	Strouhal number
u	$\mathrm{m\,s^{-1}}$	Streamwise component of flow
U_{inf}	$\mathrm{m\,s^{-1}}$	Mean flow velocity
v	$\mathrm{m\,s^{-1}}$	Spanwise component of flow
λ	mm	Serration wavelength
ρ	$\mathrm{kg\,m^{-3}}$	Water density

Non-dimensional parameters

Parameter	Value	Equation	Non-dimensional value
H	20 mm	H/H	1
λ	10 mm	λ/H	0.5
L	40 mm	L/H	2
P_L	720 mm	P_L/H	36
$D/H = 1$	20 mm	D/H	1
$D/H = 2$	40 mm	D/H	2
$D/H = 3$	60 mm	D/H	3
X	20 mm	x/H	1
Y	20 mm	y/H	1
U_{inf}	$0.03\,\mathrm{m\,s^{-1}}$	U_{inf}/U_{inf}	1
$u\,RMS$	$-\mathrm{m\,s^{-1}}$	$u\,RMS/U_{inf}$	$-$
$v\,RMS$	$-\mathrm{m\,s^{-1}}$	$v\,RMS/U_{inf}$	$-$
Re_b	600	$\rho U_{inf} H/\mu$	$-$
St	0.2	fD/U_{inf}	$-$

1 Introduction

Most owls (Strigiformes) are nocturnal. Since owls hunt mainly by hearing (Payne 1971; Konishi 1973; Hausmann et al. 2008) they need to avoid noise emission during flight (for a recent review see Wagner et al. 2017; Jaworski et al. 2020). A reduction of noise would also make it more difficult for a potential prey to hear the approaching predator (Clark et al. 2020). Morphological adaptations of the wings and the wing feathers are the basis for a silent owl flight (Graham 1934; Bachmann et al. 2007; Bachmann et al. 2011a; Wagner et al. 2017). Flight feathers are composed of a rachis, an inner vane and an outer vane, the vanes consist of barbs and barbules. One important adaptation to silent flight are serrations at flight feathers (Bachmann et al. 2011b; Weger et al. 2016). Serrations are sometimes also referred to as comb-like structures (Rao et al. 2017). In the barn owl, serrations occur specifically on primary feather 10 (10^{th} primary). This feather and its serrations form most of the leading edge of the wing which are directly exposed to airflow. Serrations are characterised by a reduction of the barbules at the apical part of barbs of the outer vane that result in a free-standing barb tip. The barb tips are bent upwards, away from the rachis (positive pitch), and are twisted (Bachmann et al. 2011b; Weger et al. 2016). Similar leading edge adaptations are also found on other bird species however, their purpose is also not yet known (Clark et al. 2020). Serrations are more pronounced in nocturnal species that mainly rely on acoustic cues during hunting than in diurnal species that more rely on vision for prey capture, indicating the importance of the serrations for noise reduction (Weger et al. 2016). Noise measurements on flying owls (Kroeger et al. 1972; Neuhaus et al. 1973; Sarradj et al. 2011; Geyer et al. 2014) and owl wings (Geyer et al. 2016b; Geyer et al. 2017) indicated that serrations reduce flight-noise. Neuhaus et al. (1973) compared noise production in barn-owl flight with intact serrations and after the serrations were cut off. These authors found that serrations reduce noise before landing but not during gliding flight. Geyer et al. (2016b) and Geyer et al. (2017) observed a reduction of flight noise by serrations at high angles of attack. Sarradj et al. (2011) reported less noise emission in a flying barn owl (*Tyto alba*) than in a common kestrel (*Falco tinnunculus*) or a harris hawk (*Parabuteo unicinctus*). The noise-reducing effect was associated with aeroacoustics of the flow along the suction side of the owl wing (Kroeger et al. 1972; Neuhaus et al. 1973; Winzen et al. 2014; Geyer et al. 2016b). In addition, possible noise sources from turbulent structures impacting the leading edge may be important, causing the so-called leading edge noise (Jaworski et al. 2020). While these studies provided some insight into the noise-reducing properties of owl wings, they were all carried out with whole wings. Therefore, the effect of the serrations could only be studied in conjunction with the other adaptations of owls to silent flight.

Apart from studying natural serrations, the influence on the airflow of simplified artificial serrations was examined (Arndt 1972; Schwind et al. 1973; Klän et al. 2010; Hansen et al. 2012; Gharali et al. 2014; Narayanan et al. 2015; Agrawal et al. 2016; Geyer et al. 2016a). For example, acoustic measurements made in turbulent airflow suggested that artificial serrations reduce noise generation (Narayanan et al. 2015; Geyer et al. 2016a). Gharali et al. (2014) reported a load increment for a serrated case in comparison to a case without serrations and a delay in dynamic stall at high angles of attack. Schwind et al. (1973) have also already noted that the geometry and the shape of the serrations influences their effectiveness. Klän et al. (2010) observed that the impact of the serrations on the flow field strongly depended on flow condition, and proposed to study the flow field in the immediate vicinity of the serrations.

What is missing so far is a more detailed investigation of how barn-owl shaped artificial serrations affect airflow, especially in the vicinity, and immediately downstream of the serrations and independently of the other adaptations to silent flight (Jaworski et al. 2020). A first approach by Muthuramalingam et al. (2020b) showed the surprising effect of an inboard flow turning induced by the serrations in a freestream flow, which was concluded to postpone transition to turbulent

flow on the wings suction side during gliding flight, supporting the aeroacoustic noise reducing effect of the serrations as discussed above. This study used models of serrations based on digital reconstruction of the micron-size natural barb structures, producing serrations with yaw, pitch and twist, closely resembling the shape of natural serrations. To further this study we use herein the same model and study it in unsteady inflow conditions. We investigate the hypothesis that incoming turbulent structures are modified by the protruding barbs when they interact with the leading edge, leading to reduced leading-edge noise. Therefore our study compares the flow details around the barbs when the inflow is uniform or when populated with vortical structures, interacting with the barbs. The flow pattern around the serrations are mapped with 2D Particle Image Velocimetry (PIV) and compared in qualitative and quantitative values, addressing the turbulence intensities in the inflow and their attenuation after passing the serrations. Lastly the power-spectra of the velocity fluctuations are presented to pass judgment on the barbs ability to attenuating flow fluctuations and acoustic noise. The paper is formatted as follows: initially the setup of the experiments is discussed, including the geometry and characteristics of the serrations being tested, see section 2. In section 3 the results are shown and discussed, starting with the effects of the individual barbs on the freestream, followed by the effects of the serrations as a whole in uniform and vortical flow. This includes the serrations attenuating the intensity of freestream turbulence and peaks in the spectral energy distribution produced by various cylinder sizes. The results are compared to other studies on owl's leading edge in section 4 and finally conclusions are given regarding their possible aeroacoustic function 5.

2 Experimental setup

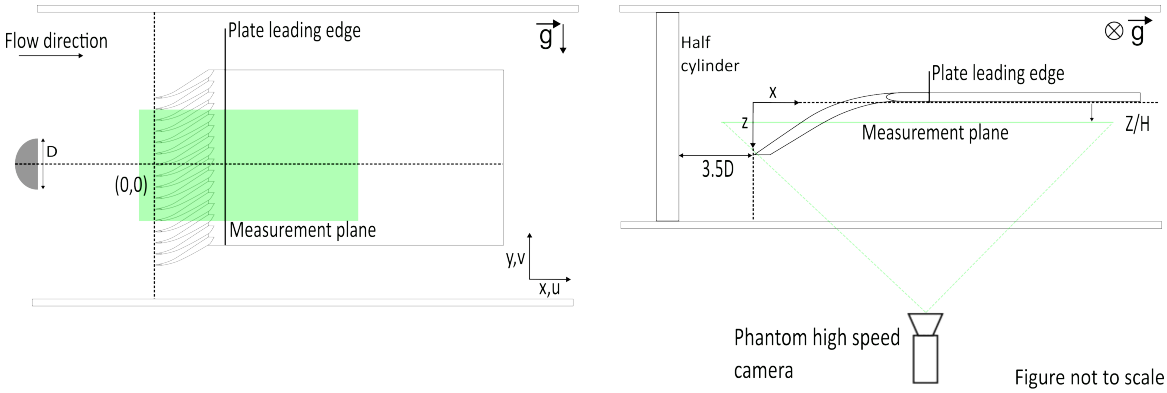

Figure 1: Setup of the serration model in the water tunnel relative to the flow direction. The half-cylinder is located $3.5D$ upstream and the measurement area (the entire field of view of the camera) is highlighted in green.

In this study we make use of the fundamental aspects of similitude in fluid mechanics, which means that the flow features and streamlines are identical for different scaling factors of the geometry as long as the non-dimensional flow parameters such as the Reynolds number and the Strouhal number are similar (Zierep 2013). For low Mach number (Ma $\leq$ 0.1) the flow is in the incompressible range and one can use e.g studies in a water-tunnel to analyse the streamlines around a wing similar as when exposed to airflow. For reasons of better experimental conditions, we used a 20-times up-scaled model of the barbs which is studied in a water tunnel using PIV (Raffel et al. 2018). The model geometry is based off the 3D-scan of the original, millimeter-scaled barbs of a *T. furcata pratincola*, see also 2.1. Therefore typical heights of the barbs of $h = 1mm$ in nature result into structures with a height $H = 20mm$ in the model. The Reynolds number built with the barb height H and the free stream velocity U_{inf} equals to $Re_b = 600$, which

corresponds to the flow conditions around the original millimeter-scaled barbs at flight velocities of about 8m/s in air, which is in the typical range of gliding flight velocities of owls (5m/s-10m/s, see Wagner et al. 2017). The tunnel was a closed loop with a honeycomb mesh located upstream of the test section. Water was seeded with small tracer particles (diameter $\approx$ 20 µm) for flow visualisation and PIV measurements. The test section with transparent walls had dimensions of 0.4 m width, 0.5 m depth and 1.2 m length. The serration model was placed in the test section so that the spanwise axis of the comb is aligned with the vertical axis and with the tips facing the flow, see fig. 1.

2.1 Model geometry of the serrations

The physical model of the leading-edge serrations used herein is the same as that introduced by Muthuramalingam et al. (2020b) where a thorough description on the development and dimensions of the model are given. It is printed with a 3D printer and attached to a planar flat plate (length $36H$, zero angle of attack) in approximation of the situation of a growing boundary layer along the first part of a wing. The idealised model has uniform barb dimensions and a constant wavelength of a $\lambda = 0.5H$ (fig. 2a,c) with a total of 32 individual barbs figs. 1 to 3). Some important features of the serrations are the taper of the barbs towards the tip, resulting in an increasing free space between the barbs towards the tip (fig. 2c). Another feature is the variation in twist with maximum twist at the root (Bachmann et al. 2011b) and zero twist at the tip (in line with the flow); this results in reducing profile area with height (fig. 2a).

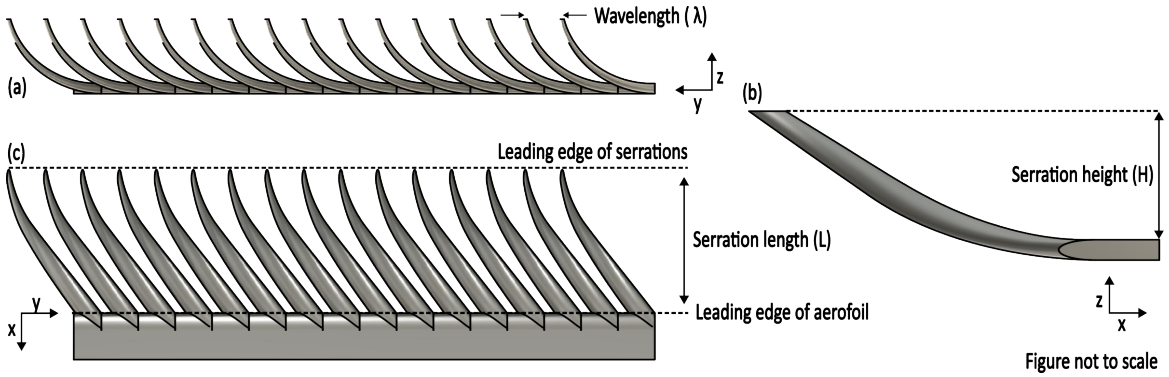

Figure 2: Orientation of the idealised serration model, showing the yaw, pitch, twist and taper of each barb. a) Front-view, looking in the direction of the flow. b) Side-view of the serrations (enlarged). c) Top-view of the serrations, looking normal to the plate surface. (geometry re-illustrated from Muthuramalingam et al. 2020b)

2.2 Uniform and turbulent inflow conditions

When freestream turbulence impacts on the leading edge of an aerofoil it is known to cause leading-edge noise (Jaworski et al. 2020). Our work is addressing the hypothesis that the serrations protruding upstream and upwards from the leading edge have an impact on the noise formation and spectral distribution. This is thought of in part as a consequence of the flow fluctuations being manipulated by the barbs before they reach the leading edge (flow preconditioning). To study this, we investigate the flow details around the barbs when the barbs are in a uniform inflow or in flow with freestream turbulence, the latter being produced by placing a cylinder upstream, producing a turbulent wake that hits the barbs. The turbulent wake of a cylinder has been studied in detail for Reynolds-numbers between 200 and 7000 and is well documented in literature (see Townsend 1947). Therefore, cylinders of different diameter ($D/H = 1, 2, 3$) were

placed upstream of the model in horizontal axis (normal to the spanwise axis of the comb) at a distance of $3.5D$ upstream of the leading edge of the barbs (figs. 1 and 3). This produced unsteady, turbulent wakes at cylinder Reynolds-numbers Re_{Cyl} of 600, 1200 and 1800. The von Karman-type wake contains large-scale coherent vortex structures, shedding in an alternating way from the edges of the cylinder at a non-dimensional frequency of approximately $St = 0.21$. In addition, small scale structures are formed, stemming from the instability of the shear layers and the formation of streamwise vortices, for a review see (Williamson 1996). This allows to study the effect of different scales of the vortical structures relative to the wavelength of the barbs (relative wavelengths are $D/\lambda = 2, 4, 6$).

2.3 PIV setup and camera arrangement

A 5 Watt continuous wave laser (Dantec Dynamics RayPower, 532 nm wavelength) equipped with light-sheet optics was positioned perpendicular to the flat plate/ serrations and underneath the tunnel test section. A 45° mirror was used to reflect the light-sheet into the test section and parallel to the surface of the flat plate (fig. 1). A Phantom Miro M310 high speed camera (1280×800 pixel sensor size) equipped with a Tokina 100 mm macro lens was used to capture the flow across the barbs. Due to the relatively low velocities used the frame rate was set to 60fps ($\Delta t = 1 \setminus 60s$) with exposure times of 5000 µs. For each measurement series the light sheet was positioned parallel to the plate surface at three different distances Z to the wall (located at 13%, 36% and 69% serration height), recording the flow in different cross-sections along the barb height.

2.4 Processing

Processing of the captured image sequences, with 1500 images per test, was done via PIVlab (Thielicke et al. 2014) followed by further post-processing of the plots on *tecplot*. The background mean intensity, determined over the entire frame and time series, was first subtracted from each of the images before being processed. Each consecutive image-pair of the sequence was processed with the method of digital cross-correlation (correlating frame n with frame n+1) in a two-pass iteration with 50% overlap of the interrogation window (the window size remained constant with $32px32px$). Image masking was applied for regions, where the barbs enter the light-sheet or in regions of shadows behind those. Note that those regions are later marked with a rectangular box in the plots and are excluded from further data analysis. The resulting velocity fields were then refined via a local median-filter to remove erroneous vectors. The freestream flow contains two velocity components, the flow in the direction of bulk flow (streamwise or in x-direction) and the flow perpendicular to the bulk flow direction (spanwise or in y-direction) (fig. 3). The resulting velocity field is of the form u,v(i,j,t) at the location x,y(i,j). The size of i_{max} and j_{max} were 63 and 47 respectively, resulting in 2961 data points across the whole measurement area.

$$u_{i,j,rms} = \frac{1}{U_{inf}} \sqrt{\frac{1}{n} \sum_{n=1}^{n} (u_{i,j,n} - \bar{u}_{i,j})^2} \tag{1}$$

The vector field was then exported to *tecplot* where the RMS values for u and v velocity components were calculated and then normalised with respect to U_{inf}. These values represent the velocity fluctuation intensities for the streamwise and spanwise component and are comparable to the values of turbulent intensities in the wake of the cylinder. A non-dimensional cutoff value of 0.3 was selected to highlight the upstream and downstream flow fluctuation intensity levels but also to allow for comparison between the different cylinder diameters. Those data are shown later as contour plots. Note that the separation into the two different velocity components allows

a separate discussion of the contribution to the total turbulence kinetic energy, which is typically used in aeroacoustics investigations to relate to acoustic noise sources.

2.5 Data extraction

Further processing was conducted to obtain algebraic values for mean RMS levels in selected regions upstream and downstream of the serrations by averaging over a field of $2H \times 2H$ using eq. (2):

$$\overline{U_{rms}} = \frac{1}{k * l} \sum_{i=1}^{k} \sum_{j=1}^{l} (u_{i,j,rms}) \tag{2}$$

The upstream RMS averaging areas were chosen based on the region of highest velocity fluctuations in the direct wake of each of the cylinders, this was $1D$ downstream of the trailing edge for the $D/H = 1$ and $D/H = 2$ cylinders and $2D$ downstream for the $D/H = 3$ cylinder, symmetric to the center line ($y = 0$). For the downstream averaging area the region was kept constant for each test located $3.5H$ downstream of the leading edge of the barbs (fig. 3).

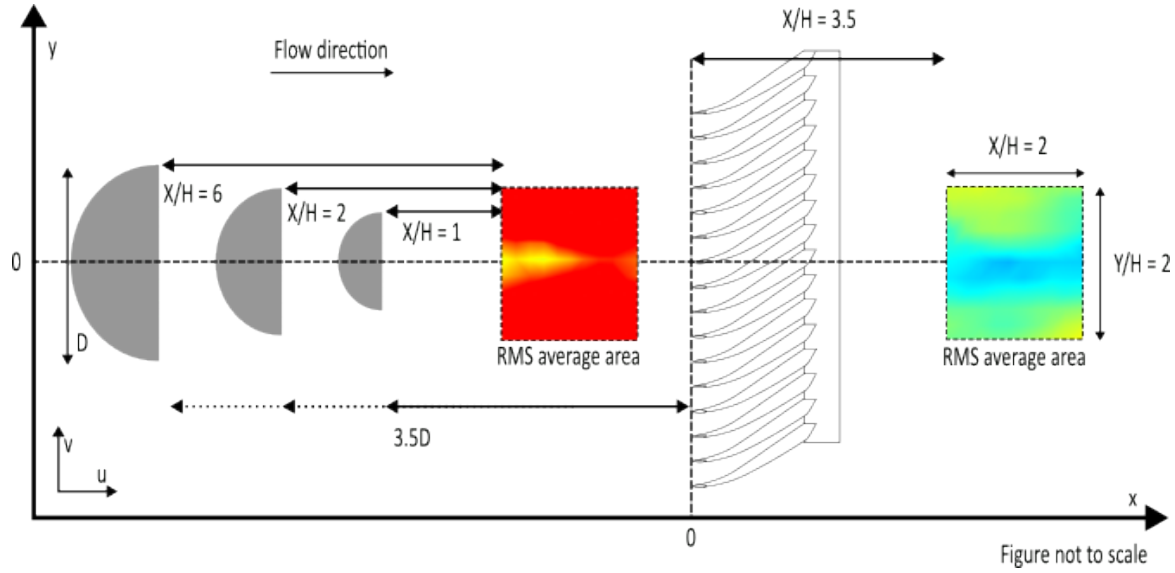

Figure 3: RMS averaging areas for the three cylinders relative to the leading edge of the serrations and normalised with respect to barb height; note that the upstream measurement area is dependent on cylinder diameter.

3 Results

All geometrical parameters herein were normalised by the serration height H (fig. 2) or wavelength λ and the velocities are referenced to U_{inf}. The origin of the axes in the contour plots is always at the tip of the barbs, which is indicated by a black dashed line in the following figures figs. 4, 6 to 9, 14 and 15. The bulk flow direction is left to right, where the positive X-direction is downstream. Herein the configurations are labelled with respect to the cylinder located upstream '$D/H = 1, 2, 3$', the percentage z/H where the measurement plane was located, and an additional postfix, which is 'P' for the plain case of only the flat plate in the flow and 'B' for the flat plate with the leading edge barbs attached.

3.1 Baseline flow

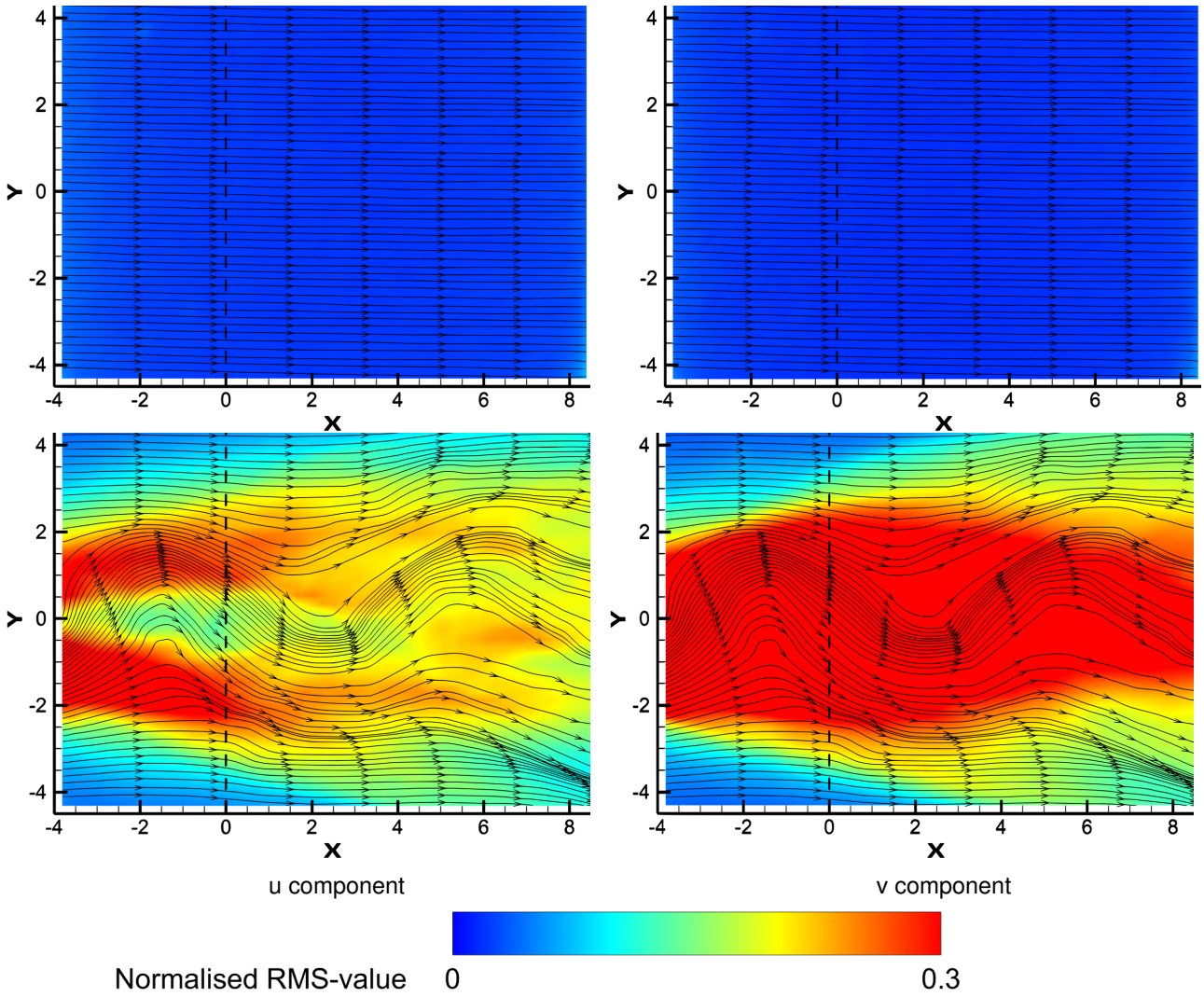

Figure 4: Contours of velocity fluctuation intensity of u-component (left) and v-component (right) in uniform flow (top row) and in the wake of a D-shaped cylinder (bottom row), overlaid with instantaneous streamlines. The dashed black line is where the leading edge of the serrations would be located.

Initial measurements of the empty tunnel were taken to confirm the set freestream velocity and to establish the baseline turbulence of the tunnel. The mean RMS level of the tunnel in the measurement area was $4.03 \times 10^{-4} \pm 1.95 \times 10^{-5} SD$ (u-component) and $3.39 \times 10^{-4} \pm 2.47 \times 10^{-5} SD$ (v-component), resulting in a freestream turbulence level of approximately 1.39% (u) and 1.16% (v). Figure 4 top row, demonstrates the low RMS values in both velocity components across the whole measurement area and also the instantaneous flow field (roughly uniform horizontal streamlines) overlaid. This shows that the flow within the tunnel is laminar and uniform. Therefore any flow fluctuations seen in the following figures are a result of the barbs and cylinder wakes. Figure 4 bottom row is included to demonstrate how the contours of the time-averaged fluctuation intensities differ from the instantaneous flow field (streamlines) in the wake of the cylinder. From the overlaid instantaneous streamlines alternating vortex shedding from each side of the half-cylinder is observed, representing the vortex pattern in a typical von Karman vortex street. Through time-averaging this pattern is lost. The regions of high u- and v-component fluctuations are easily identifiable, thus enabling quantitative analysis of the serrations effect.

Additional PIV measurements were captured directly in the wake of the D-shaped cylinders

(see appendix, fig. 13). The fluctuation intensities for both components (u and v) were large in the vortex street, increasing in magnitude with cylinder diameter. The average intensity levels for the $D/H = 1, 2, 3$ cylinders were 26.8% and 54.6%, 38.3% (u-component) and 56.2%, 37.3% and 54.6% (v-component) respectively. The time-averaged contours show the full extension of the wake and approximate symmetry to the central axis. Additional measurements further downstream of the cylinder wake in the location of where the barbs would be located were also taken (see appendix, fig. 14). The $D/H = 1, 2$ wakes reached a uniform thickness by the leading edge location of the barbs however, for the $D/H = 3$ cylinder the wake is still increasing in size at this location. For the v-component the RMS values remained above 0.3 until $6H$ downstream of the serrations for the smallest cylinder and beyond the measurement area for the two larger cylinders. For the u-component the fluctuations began to diminish below values of 0.3 around the leading edge location (see appendix, black dashed line fig. 14).

Finally the flat plate was placed in the tunnel without the barbs and the flow was measured in wall-parallel planes with each cylinder upstream (see appendix, fig. 15). The contours of RMS values for both velocity components are comparable to those of the plain cylinder wake, which let us conclude the existence of the plate in the wake of the cylinder has minimal effect on the flow structures when passing by.

3.2 Near-wake flow at the serrations

The Reynolds number built with the height of the barbs is sufficiently high (when compared to a simplified cylinder) to induce vortex shedding and shear layers downstream of the structure of the barbs themselves. Therefore measurements were first taken with uniform inflow conditions to quantify their wake impact locally. The setup remained the same as in the other tests. To achieve higher spatial resolution, the high speed camera now was equipped with a 300 mm lens and the frame rate was increased to 120 fps. The resulting field of view with the larger lens was $2.5H \times 3.5H$ which captured the wake of 5 serrations at 50%H. From fig. 5 no stronger flow fluctuations can be observed in either the u- or v-component. However, a velocity reduction is seen downstream of each individual barb, indicating the immediate wake of the barbs. In the free space between the barbs higher streamwise velocities are seen, which stems from the accelerated fluid flow in the gap. The shear layers formed between those high-and lower speed regions (fig. 5 RMS plots) diminish quickly, within 0.5H in both velocity components, leaving a streaky flow pattern, aligned with the regular spacing of the barbs in the comb. This pattern is also observed in the uniform flow test with larger field of view (fig. 6), particularly at lower Z, and best visible in the contours of the u-component. To further demonstrate the longevity of the streaked flow, fig. 5 also shows the time-average velocity profiles at selected distances $X = 1$, $X = 2$ and $X = 3$. Within the higher RMS region ($X = 1$) the velocity is accelerated in the spacing between the barbs and reduced in the wake of the barbs, resulting in the quasi-harmonic modulation of the streamwise velocity profile. Further downstream ($X = 2.0$) the effect is still present but reduced in magnitude while it is almost indistinguishable at $X = 3$. Notably, over the sampling locations the velocity profiles also become shifted in phase which originates from the flow turning effect caused by the serrations, which bends the streamlines upwards (see Muthuramalingam et al. 2020b).

3.3 Serrations in uniform and vortical inflow

- Uniform inflow: Figure 6 shows the effect of the serrations for different wall-parallel planes along the height of the barbs in larger view (uniform inflow). Due to the barbs being an obstructing body to the incoming flow, fluctuations in both velocity components are most noticeable at lower heights (Z=13% and Z=36%). Here, the barbs are more curved with

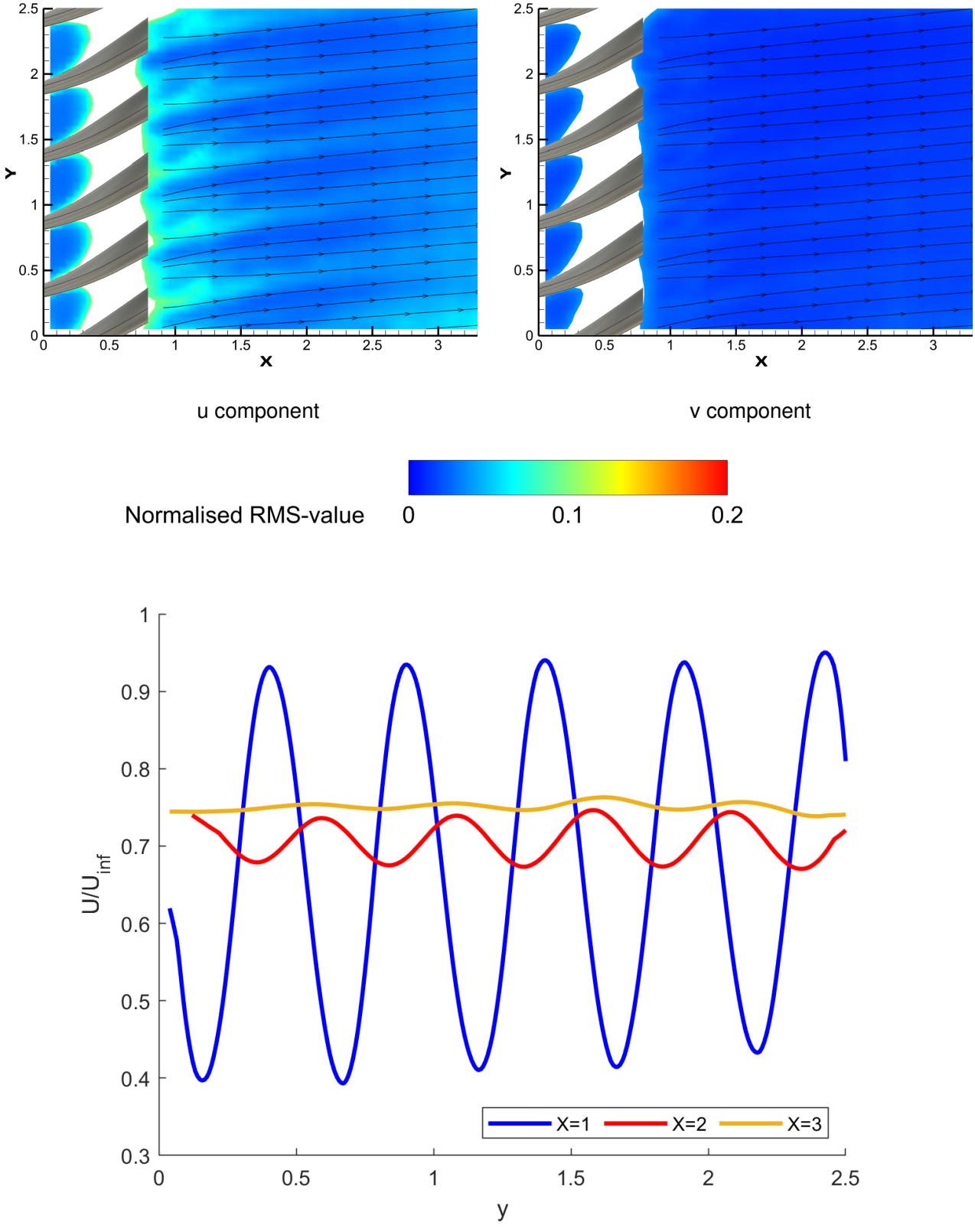

Figure 5: Near wake velocity fields and streamwise velocity profiles. Contour plots of velocity fluctuation intensity of u-component (left) and v-component (right) in the direct wake of the serrations at uniform inflow at $50\%H$. The serrations are overlaid for reference and the shadowed regions have been masked. Below, the corresponding normalised, time-averaged streamwise velocity profiles along the span of the comb at $X = 1, 2$ and 3.

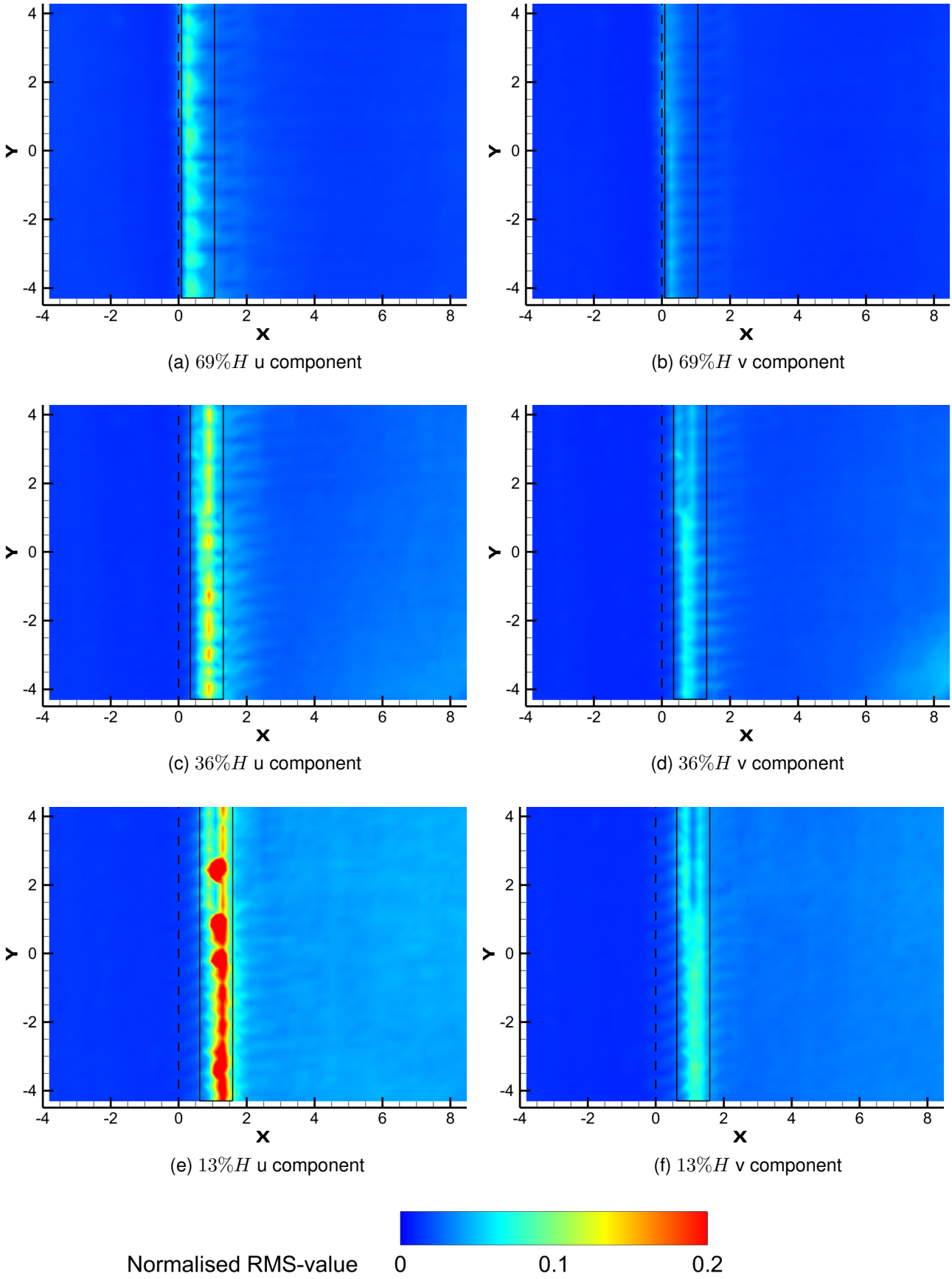

(a) $69\%H$ u component

(b) $69\%H$ v component

(c) $36\%H$ u component

(d) $36\%H$ v component

(e) $13\%H$ u component

(f) $13\%H$ v component

Figure 6: Contour plots of velocity fluctuation intensity for the u-component (left column) and v-component (right column) along the serrations in uniform inflow. Dashed black line indicates the location of the tips of the barbs. The black rectangle is where the light sheet crosses the barbs, resulting in some shadows and spurious vectors (particularly evident in c and e) which are not flow features.

respect to the freestream and have thicker cross sections, resulting in increased frontal areas and therefore a reduction in velocity directly downstream of each individual barb. At Z=69% height, this effect diminishes as the curvature of the barbs reduces to be more parallel to the freestream and the cross section tapers, resulting in reduced perturbations from the mean velocity. The RMS values at all heights were consistently higher in the mean flow direction than in the spanwise flow direction. At all barb heights the effects on the flow are limited to the immediate area around the serrations. Again, the flow turning effect observed in (Muthuramalingam et al. 2020b) can be seen here too, showing the inclination of the streaked pattern (fig. 6). In all cases, the effects wane beyond 2 barb heights ($X = 2$) downstream; beyond $X = 2$ the flow is rather uniform and comparable to the flow upstream, except from the observed turning effect.

- Freestream turbulence: When the cylinder is placed upstream of the serrations, a strong dampening of the incoming fluctuations is observed once they have passed the barbs, seen in the reduction of the peak RMS values, both for the u- and v-component figs. 7 to 9b,d,f. This is consistent for all the tested cylinder diameters, where the fluctuation intensities can be seen to be reduced to similar levels at each respective height (view figs. 7 to 9 b,d,f respectively). For 13% and 36% barb height the RMS values of the v-component are reduced below the 0.3 threshold immediately downstream of the barbs and continue to decrease downstream. Overall, the barbs are more effective at reducing the fluctuation intensities in the spanwise v-component than in the u-component. Note also that the transition to lower fluctuation intensities is rather sharp and happens immediate behind the cross-sectional plane of the barbs (which is always upstream of the leading edge of the plate).

  The regions of larger fluctuations in both velocity components also show in some cases a streaky pattern, particularly at the mid to lower heights tested (figs. 7 to 9a,c,d), indicating again the overall flow turning effect caused by the serrations. The observed effect diminishes when moving further away from the wall along the height of the barbs, where the curvature decreases, the barbs narrow and therefore, the free gap between the barbs increases. Nevertheless regardless of height, compared to the plain plate in the cylinder wake (see fig. 15 in the appendix) and the cylinder wake alone (see fig. 14 in the appendix), the fluctuation intensity levels are largely reduced downstream of the barbs. Overall, the serrations can be understood as acting as a flow straightener to the incoming vortex street, with a diminishing effect when moving from the root to the tip of the barbs.

3.4 Mean fluctuation intensities

The mean RMS values, taken as an average over the above defined regions of interest, are compared to each other to give an indication of mean fluctuation intensities in the wake. Figure 10 illustrates the effect of the different objects placed downstream of the cylinder (measurement plane at 33.4%H). The presence of the flat plate has negligible effect on the fluctuation intensities, similar to the natural diffusive decay of fluctuation intensities in the plain cylinder wake. This decay is calculated to about 25.3% (u) and 33.4% (v) for the small cylinder, 47.0% (u) and 30.5% (v) for the medium cylinder and 46.7% (u) and 24.8% (v) for the large cylinder. Similar values are obtained when the plate is inserted (26.1% / 44.5% in u,v for the small cylinder, 47.9% / 28.9% in u,v for the medium cylinder and 60.2% / 21.5% in u,v for the large cylinder). In contrast, with the leading edge serrations attached a noticeable reduction in fluctuations occurs for all the cylinders tested, specifically seen for the v-component.

Figure 11 compares the attenuation effect for the different heights along the barbs. Of particular interest is the reduced fluctuation intensity levels for all the cylinder wakes, even at scales

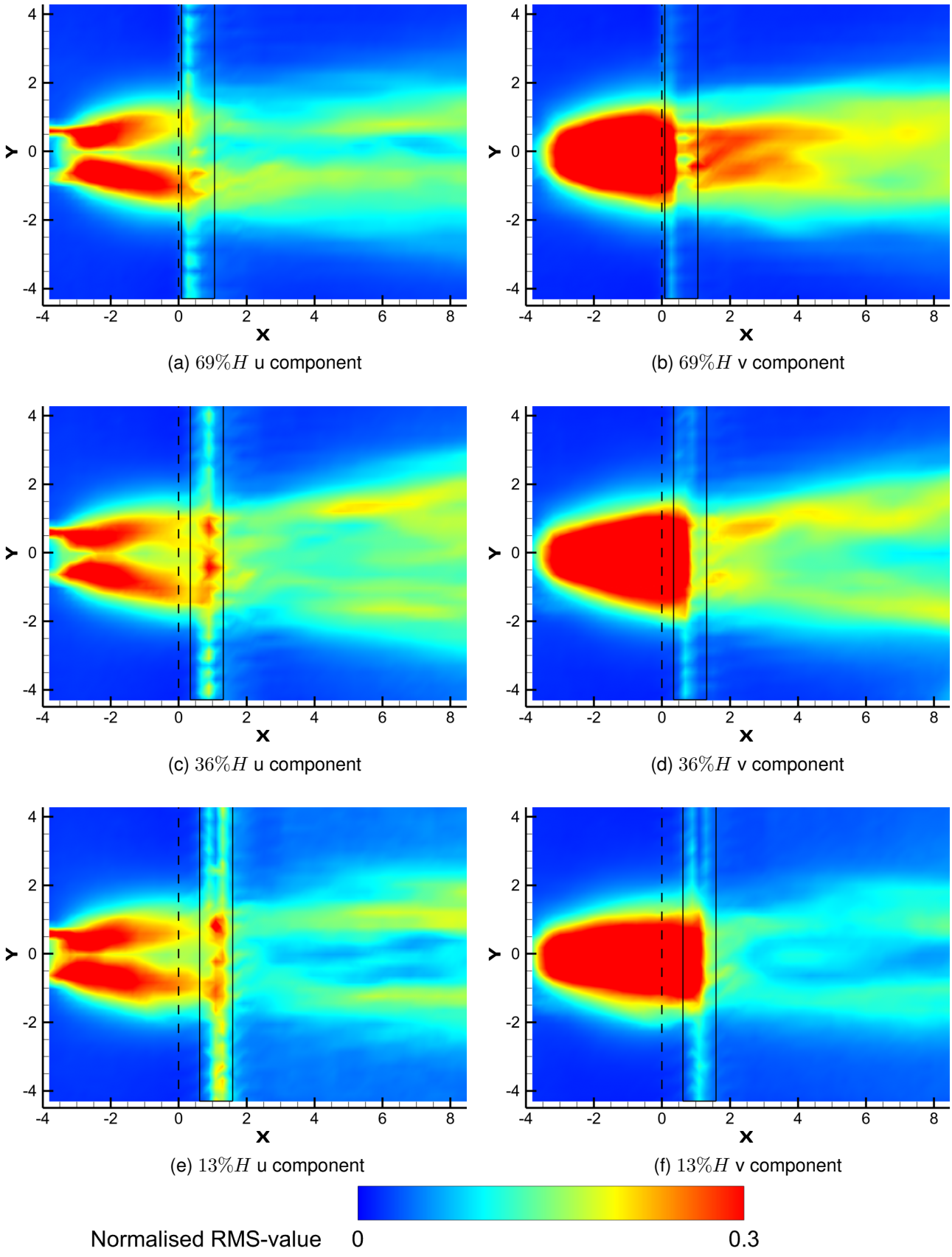

(a) $69\%H$ u component

(b) $69\%H$ v component

(c) $36\%H$ u component

(d) $36\%H$ v component

(e) $13\%H$ u component

(f) $13\%H$ v component

Figure 7: Contour plots of velocity fluctuation intensity in u-component (left column) and v-component (right column) along the serrations in the wake of a D-shaped cylinder ($D/H = 1$). Dashed black line indicates the tips of the barbs. The black rectangle is where the light sheet crosses the barbs, resulting in some shadows and spurious vectors (particularly evident in c and e) which are not flow features.

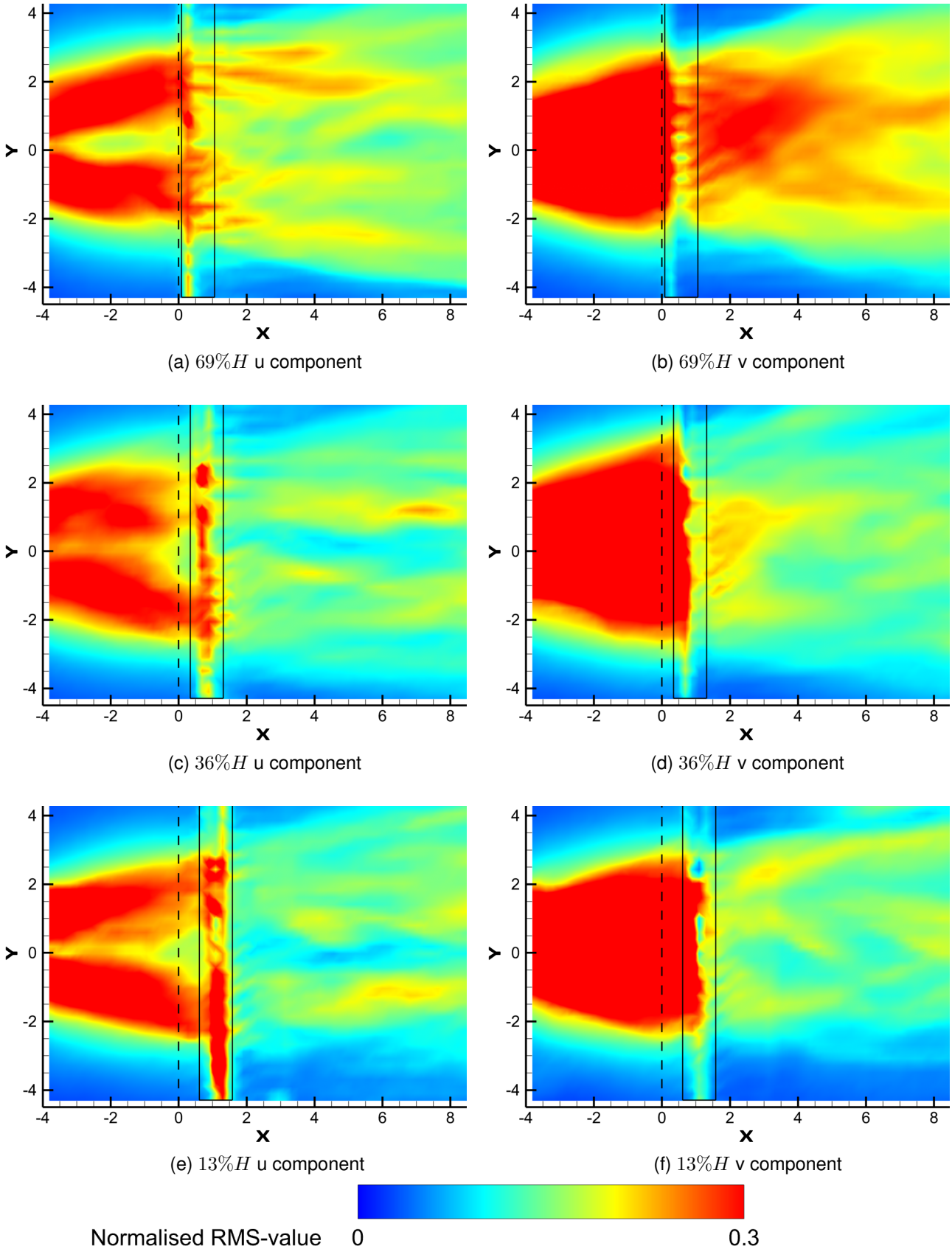

(a) $69\%H$ u component

(b) $69\%H$ v component

(c) $36\%H$ u component

(d) $36\%H$ v component

(e) $13\%H$ u component

(f) $13\%H$ v component

Figure 8: Same as fig. 7, but now in the wake of the $D/H = 2$ cylinder.

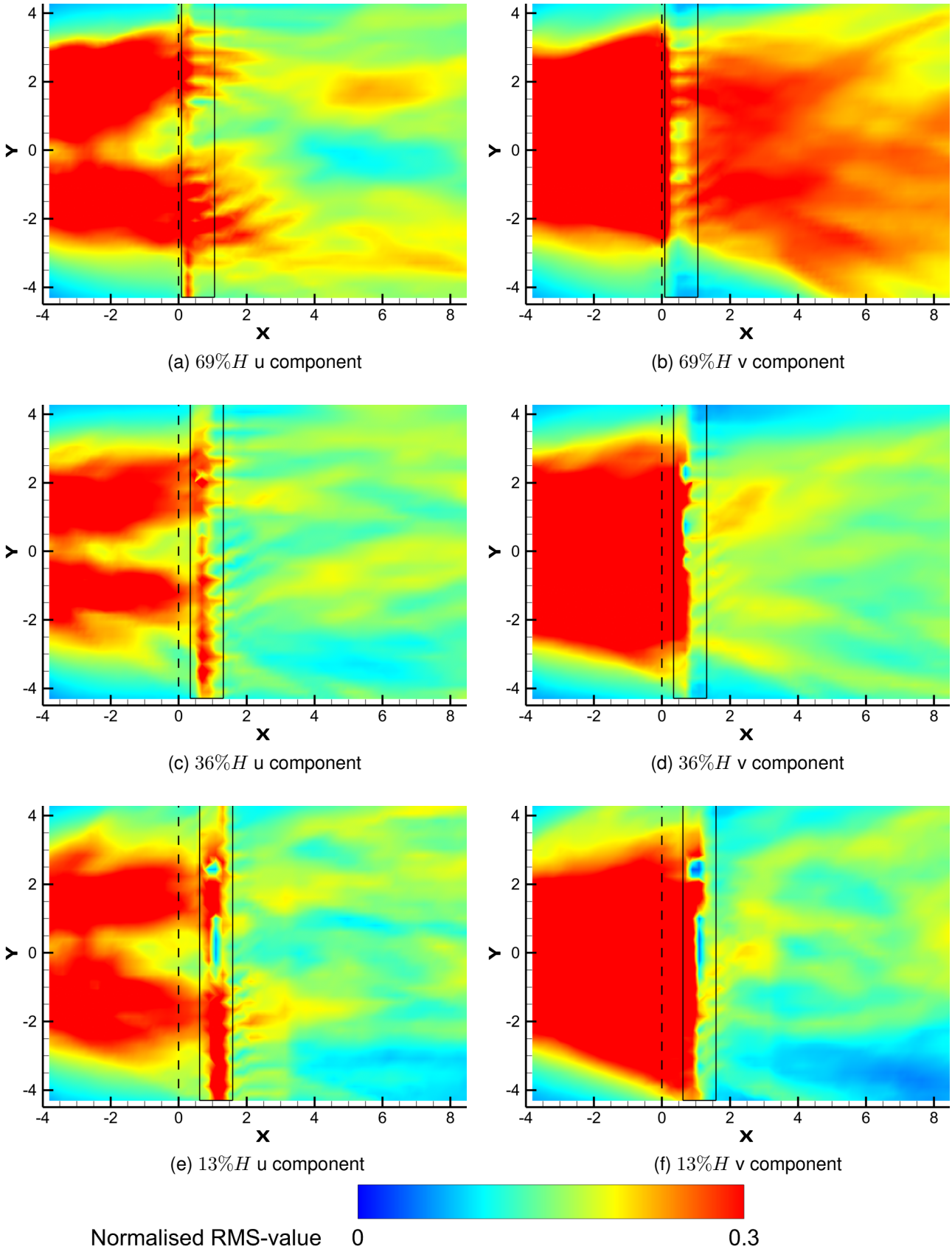

(a) $69\%H$ u component

(b) $69\%H$ v component

(c) $36\%H$ u component

(d) $36\%H$ v component

(e) $13\%H$ u component

(f) $13\%H$ v component

Figure 9: Same as fig. 7, but now in the wake of the $D/H = 3$ cylinder.

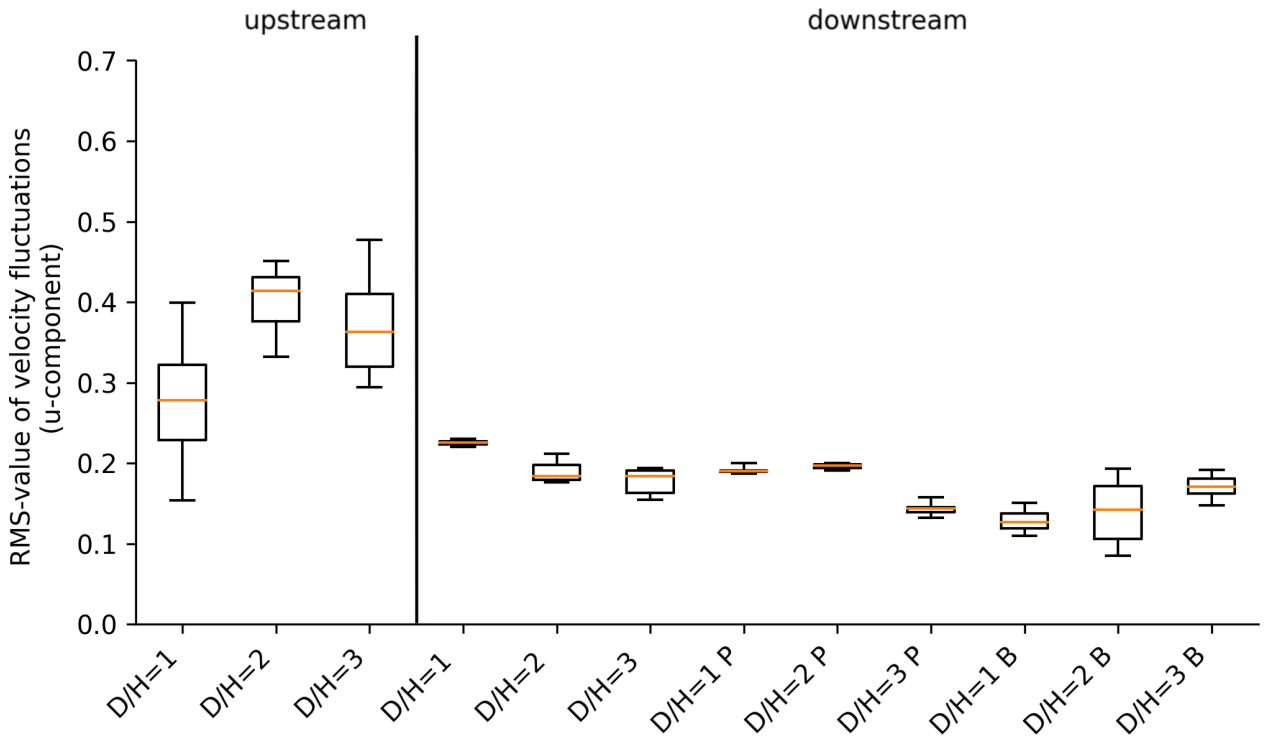

(a) u-component

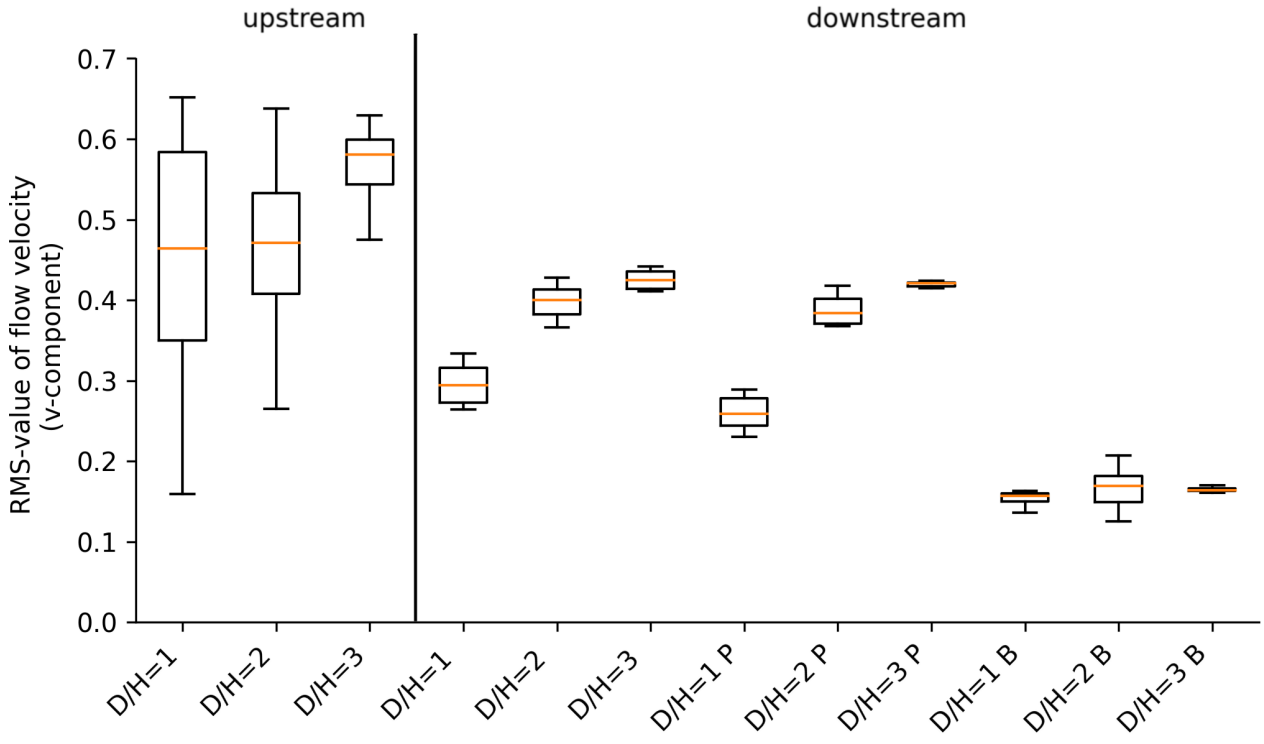

(b) v-component

Figure 10: Box and whisker plots of spatial averaged fluctuation intensities at Z=36%H, comparing upstream and downstream location area in the wake of the cylinders. Postfix 'P' denotes the plate in the wake of the cylinder, 'B' denotes the plate with the barbs attached to the leading edge in the wake of the cylinder and the absence of a postfix denotes only the cylinder is present in the flow.

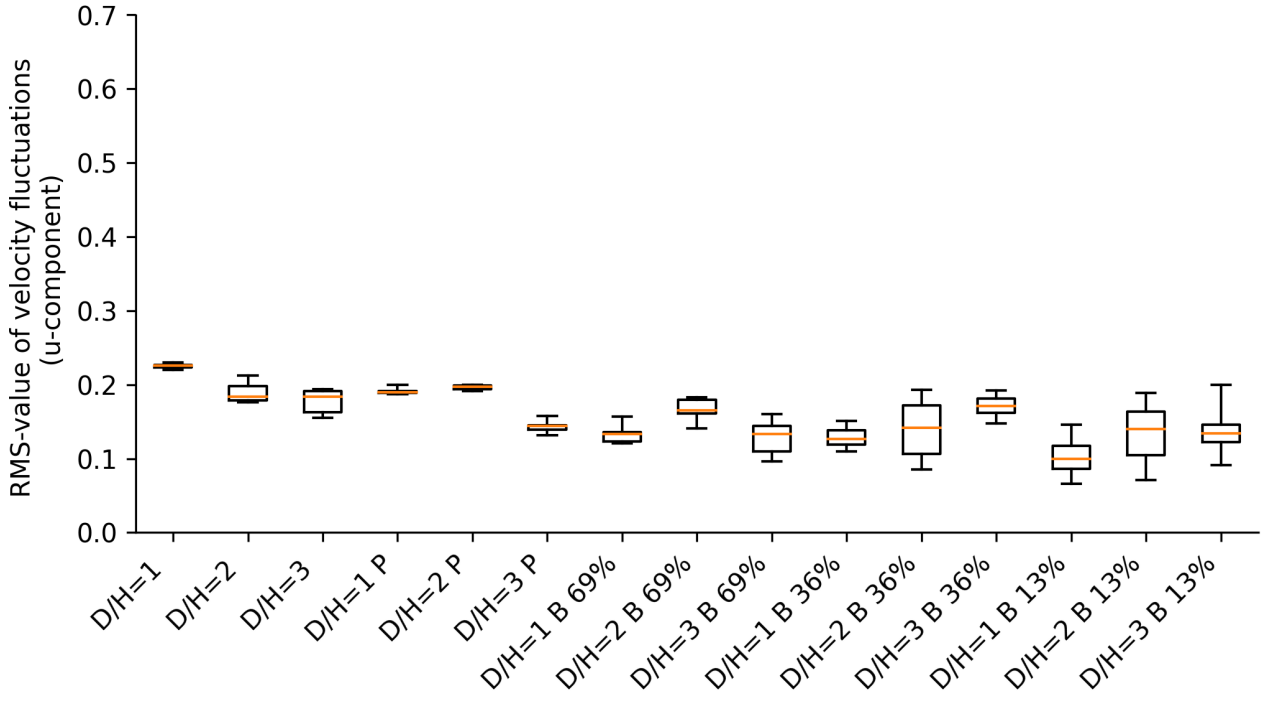

(a) u-component

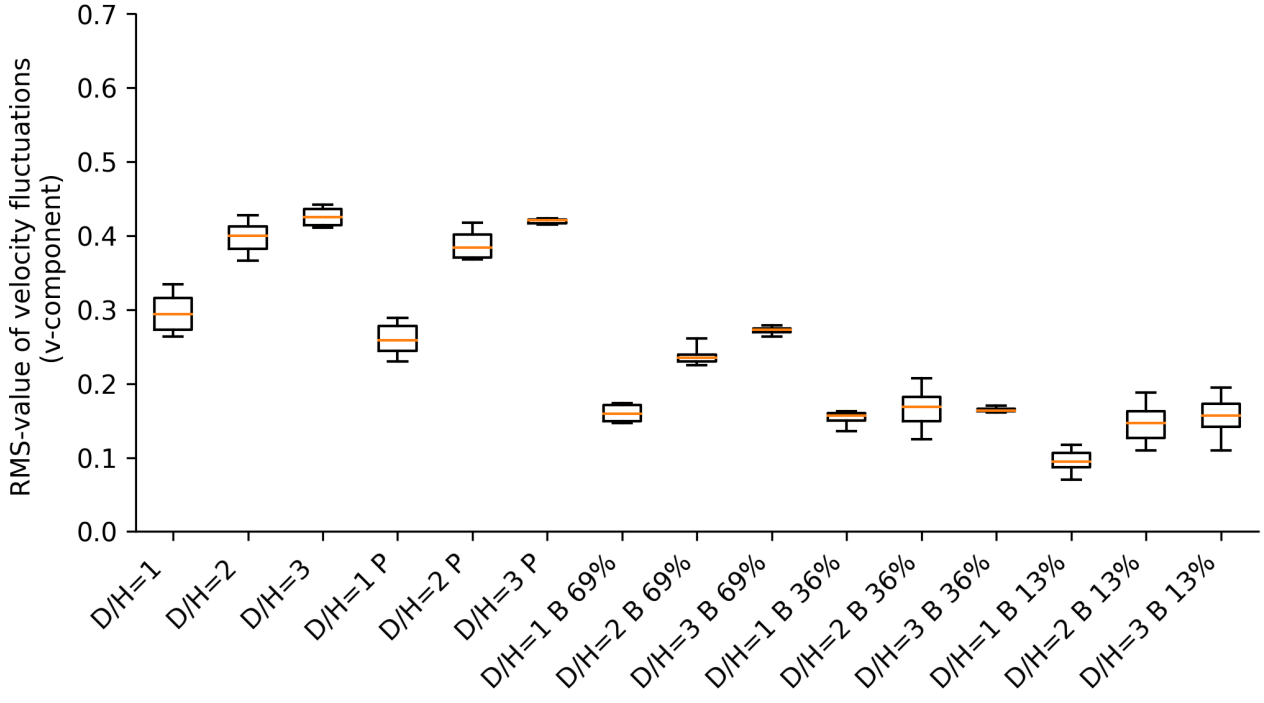

(b) v-component.

Figure 11: Spatially averaged fluctuation intensities downstream of the barbs in the different measurement planes (Z=13%H, 36%H, 69%H). Postfix 'P' denotes the plate in the wake of the cylinder, 'B' denotes the plate with the barbs attached to the leading edge in the wake of the cylinder and the absence of a postfix denotes only the cylinder is present in the flow.

comparable to the wavelength of the serrations. As in fig. 10a the streamwise turbulence intensities at all heights are moderately damped, while more pronounced decay is seen for the spanwise turbulence intensities, which clearly increases when moving from the tip to the root of the barbs. This can also be observed with the smallest cylinder ($D/H = 1$) where the mean RMS level is considerably reduced at Z=13%.

A measure to show the impact level of the barbs on the turbulence intensities is given in the following table in percentage of reduction of the mean fluctuation intensities (v-component) relative to the reference case, which is the plain plate configuration. The reduction levels for each test case are listed in table 1. It is observed that across all serration heights the percentage decrease in fluctuation intensity is comparable for each cylinder. It is also evident that the barbs are similar effective in dealing with the different scales of the vortices. Further, the table also includes the reduction in the energy along the dominant peak in the Power Spectral Density distribution (PSD) of the velocity fluctuations, which correlates with the vortex shedding frequency (≈ 0.21 for the three cylinders). The PSD is shown in fig. 16 for the data at 36%H and the large cylinder $D/H = 3$ cylinder (fig. 12, for the other cylinders see the appendix figs. 12 and 16 and table 1).

	$D/H = 1$			$D/H = 2$			$D/H = 3$		
	13%	36%	69%	13%	36%	69%	13%	36%	69%
Strouhal number peak	0.23	0.20	0.21	0.21	0.22	0.20	0.24	0.21	0.23
dB reduction	29.0	16.8	1.37	7.9	6.0	1.3	13.7	12.6	6.4
$\overline{(v')^2}$ reduction (%)	90.0	82.8	47.7	84.2	72.7	53.5	86.0	84.2	59.6

Table 1: Reduction of fluctuation energy in the PSD corresponding to the dominant peak at the vortex shedding frequency, together with percentage reduction in fluctuation intensity (v-component). All taken downstream of the serrations and relative to the same location (Z=36%). All Strouhal numbers have been calculated with respect to the cylinder diameter.

The presence of the serrations exhibit a broadband decrease in fluctuation intensity (fig. 12), particularly in the region of $St = 10^0 - 10^1$. The energy of the dominant peak is reduced at maximum levels of about 30 dB for the smallest cylinder while still at levels of 13 dB for the largest one at the plane closest to the wall. Overall, the results show that the barbs are dampening incoming flow fluctuations over a larger frequency range.

In summary, our results suggest that serrations of *T. furcata pratincola* control flow in two ways. In steady inflow, the serrations create small-scale turbulences in their wakes which rapidly dissipate downstream while the flow remains in laminar state behind the serrations. A flow turning effect is seen as previously observed in (Muthuramalingam et al. 2020b). In freestream turbulence, the serrations facilitate the reduction of flow fluctuation intensities (predominant in spanwise direction) immediately downstream of the barbs, leading to a flow homogenization while the overall flow turning effect remains intact. The results let us conclude that the presence of the forward protruding barbs could mitigate the leading edge noise by attenuating the fluctuations from incoming turbulence before they reach the leading edge. Due to the large pitch of the barbs against the incoming flow direction it is expected that similar attenuation characteristics as observed for the spanwise component persists also for the wall-normal velocity component. The latter is relevant for attenuation of leading edge noise by means of porous surfaces, see Zamponi et al. 2020.

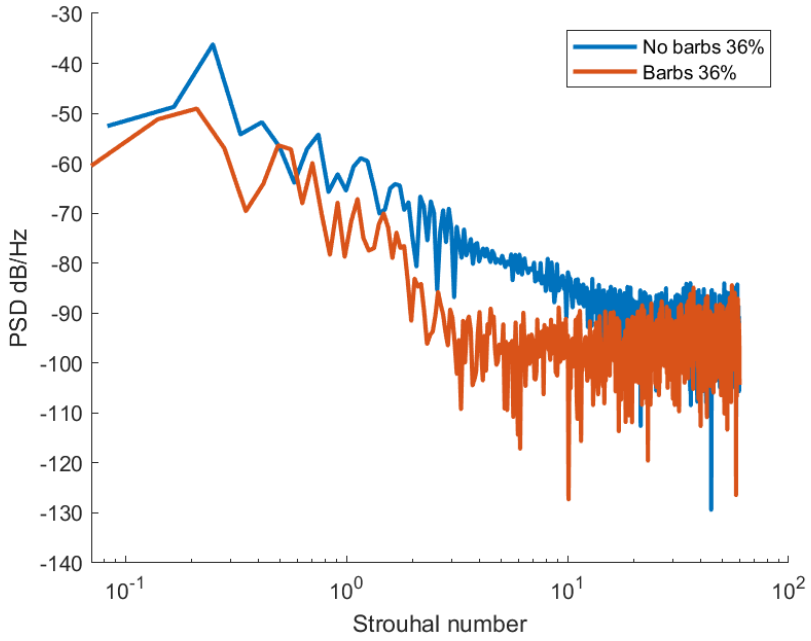

Figure 12: Spectral distribution (PSD) of velocity fluctuation energy at Z=36% in the wake of the D/H=3 cylinder (v-component). The plain plate without the barbs is used as the reference. Results for the other cylinders and Z-positions can be found in the appendix, fig. 16.

4 Comparison with other results

Natural serrations have different shapes that depend on the lifestyle (Sick 1937; Weger et al. 2016) and the position on the vane of owls (Bachmann et al. 2011b). Earlier studies had stressed the influence of the shape of the serrations on their function (Schwind et al. 1973). We put emphasis on dissecting the effects imposed by aerofoils from those imposed by serrations. The model we used consisted of an idealised, uniform barb leading edge attached to a flat plate. Specifically, our model replicates the pitch, yaw, twist and taper of the natural barbs while it did not replicate the downstream surface of natural feathers, including their velvet-like dorsal surface and their fringed trailing edge. Thus, the effects on the flow we observed were solely due to the serrations and not due to other possible adaptations of owl feathers. Our data suggests that the 3D shaped barbs provide passive flow control through stimulating laminar flow on the upper wing surface (Kroeger et al. 1972) in steady flow through the streaked flow (fig. 5) and through the flow turning (Muthuramalingam et al. 2020b). Streaked flow, similar to what is created by the serrations, have been shown in other nature inspired studies (for example fish scales, Muthuramalingam et al. 2020a) to delay transition. Previous studies have shown that serrations indeed can be shown to be effective by suppressing turbulence (Muthuramalingam et al. 2020b; Saussaman et al. 2023) on a wing at higher angle of attack. While we could not observe such effects because our investigation was restricted to the leading edge, the observed passive control by the serrations is expected to be of benefit also further downstream along the wing when the boundary layer has further developed.

Additionally to the effects of serrations in steady flow, we observed a reduction of flow fluctuation intensities behind the barbs in freestream turbulence, demonstrating the ability of the barbs to dampen flow fluctuations of various frequencies and size , even down to the wavelength of the barbs. This demonstrates that the protruding barbs by themselves have the capability to reduce flow fluctuations before impacting with the leading edge, which is one of the main sources in leading-edge noise generation. Reduction of flow fluctuations induced by serrations, therefore, may contribute to overall noise reduction. This conclusion is broadly consistent with the results

of Geyer et al. 2016b; Geyer et al. 2016a; Geyer et al. 2017.

We also observed a variation of the attenuation effect across the height of the serrations in each of the measurement series (figs. 7 to 9). This means that the three-dimensional geometry of the serrations (pitch, yaw, taper and twist) is an important morphological characteristic of barn-owl serrations. This discriminates barn-owl serrations from barbs of diurnal owls (Weger et al. 2016) and suggests that barn-owl serrations are more effective in reducing flow fluctuation intensities than the less well developed serrations of diurnal owls. If so, this would also mean aerodynamic and noise measurements with flat artificial serrations, as they were typically used so far (Arndt 1972; Schwind et al. 1973; Hersh et al. 1974; Ito 2009; Klän et al. 2010; Gharali et al. 2014; Winzen et al. 2014; Narayanan et al. 2015) did not reveal the full possible effect of serrations, as was demonstrated herein. In addition, the spectral distribution of the fluctuation energy shows the attenuation effect over a large range of frequencies, probably also relevant for the perception of prey.

5 Possible function of serrations in owl flight

That owl primaries have serrations has long been noted and related to noise reduction (Graham 1934; Sick 1937). In the following we like to speculate about the possible functions of the serrations in flight by integrating the data reported here with earlier data. We do know that serrations alter the flow under steady and unsteady flow conditions (Neuhaus et al. 1973; Ito 2009; Klän et al. 2010; Winzen et al. 2014; Narayanan et al. 2015; Geyer et al. 2016a). But how this reduces flight noise is still not known. Neuhaus et al. 1973 found a noise reducing effect shortly before an owl lands. Other findings (Sarradj et al. 2011; Geyer et al. 2013; Geyer et al. 2014; Geyer et al. 2016b; Geyer et al. 2016a; Geyer et al. 2017) suggest a noise reduction during gliding flight. Furthermore, the noise-source distribution at the wing of a barn owl shifted towards the wing tip when the serrations were removed (Geyer et al. 2017). The influence of serrations on the flow field, as demonstrated in the present study, shows that the forward protruding serrations reduce velocity fluctuations before reaching the leading edge of the wing. This may reduce possible leading edge noise emission from impacting turbulent structures, a result which adds another source to the so far supposed dominant factor of trailing edge noise as the major aspect in silent owl flight (Williams et al. 1970; Lilley 1998; Sarradj et al. 2011). We further speculate that leading-edge serrations generate a fairly constant flow profile during flapping flight. This may cause a reduction in flight noise during flapping flight or during turning and breaking maneuvers. During these maneuvers, the vortex pattern around the wing changes, as found in other bird species (Norberg 1990; Hedenström et al. 2006; Tobalske et al. 2009; Lentink et al. 2010; Muijres et al. 2012; Crandell et al. 2015). Serrations might reduce the intensity of vortices, for example, the bound vortex shed during the stopping maneuvers before striking prey. The results about the function of serrations in freestream turbulence further show that serrations can attenuate fluctuation intensities of different scales. These findings agree with measurements on noise emission of stationary aerofoils where artificial serrations led to a lower noise radiation in unsteady flow (Narayanan et al. 2015; Geyer et al. 2016a).

6 Conclusion

In this study, we provide results on the interaction of reconstructed models of leading-edge serrations of a *T. furcata pratincola* 10th primary feather with uniform flow and freestream turbulence. The results show that the serrations, as found at the *T. furcata pratincola* wings, may help with maintaining laminar flow on the suction side of the wing downstream of the serrations. This func-

tion might help with preventing the occurrence of noisy aerodynamic structures at posterior wing parts that are a major noise source during flight (Williams et al. 1970; Lilley 1998). In addition the forward protruding serrations may also contribute to reducing leading-edge noise in turbulent environments by attenuating the fluctuations when they are passing the barbs. The influence on the airflow in changing flow conditions is critical in nature, where a hunting owl has to remain silent until right before the strike. Serrations that can ”filter” out flow fluctuations or even enable laminar flow on moving or rotating wings, as it occurs when the owl starts the striking maneuver, provide a major advantage for the hunt.

Our investigation focused on the highly developed serrations of the nocturnal *T. furcata pratincola* (Bachmann et al. 2007; Bachmann et al. 2011b; Bachmann et al. 2011a). Serrations in this species are bend in three-dimensional space: they are curved towards the incoming flow, yawed and twisted. In contrast, serrations of owl species that are more diurnal like *A. noctua* have less pronounced, shorter and flatter serrations (Weger et al. 2016). It would be interesting to compare our results to models with simpler serrations, because such experiments may reveal the importance of the exact replication of the shape of the serrations when conclusions are drawn from studies with less level of geometrical detail.

7 Outlook

The current study is a follow-up study with models mimicking natural barb geometries (with pitch, yaw, twist and taper) to understand the noise emission on owl-inspired wings with leading edge serrations in turbulent flows. The use of an enlarged scale of the models allows to look into the flow details around the barbs with high resolution, otherwise not possible within original scale. The results focused on the local regions around the barbs and the observed attenuation effect of incoming flow fluctuations. Acoustic measurements with a $1:1$ scale model in an anechoic tunnel would further clarify the potential of these attenuation effects on the noise suppression of the serrations. In addition, further measurements need to include also natural geometries of the wing under variations of the angle of attack, simulating the situation during heaving and pitching motions of the bird's wings, which is part of future work.

Acknowledgements

The position of Professor Christoph Bruecker is co-funded as the BAE SYSTEMS Sir Richard Olver Chair and the Royal Academy of Engineering Chair (grant RCSRF1617/4/11) which is gratefully acknowledged. Alden Midmer is co-funded by City, University of London and BAE SYSTEMS which is gratefully acknowledged. Hermann Wagner and Matthias Weger were supported by RWTH Aachen University. Matthias Weger would also like to acknowledge the assistance given by Adrian Essert during the initial experiments conducted in Bonn University.

References

Agrawal, B and Sharma A (2016). “Numerical investigations of bio-inspired blade designs to reduce broadband noise in aircraft engines and wind turbines”. In: *54th AIAA aerospace sciences meeting*, p. 0760.

Arndt, R (1972). “Effect of leading edge serrations on noise radiation from a model rotor”. In: *Society of Naval Architects and Marine Engineers, and US Navy, Advanced Marine Vehicles Meeting*, p. 655.

Bachmann, T, Mühlenbruch G, and Wagner H (2011a). “The barn owl wing: an inspiration for silent flight in the aviation industry?” In: *Bioinspiration, Biomimetics, and Bioreplication*. Vol. 7975. SPIE, pp. 142–155.

Bachmann, T and Wagner H (2011b). “The three-dimensional shape of serrations at barn owl wings: towards a typical natural serration as a role model for biomimetic applications”. In: *Journal of anatomy* 219.2, pp. 192–202.

Bachmann, T, Klän S, Baumgartner W, Klaas M, Schröder W, and Wagner H (2007). “Morphometric characterisation of wing feathers of the barn owl Tyto alba pratincola and the pigeon Columba livia”. In: *Frontiers in zoology* 4, pp. 1–15.

Clark, CJ, LePiane K, and Liu L (2020). “Evolution and ecology of silent flight in owls and other flying vertebrates”. In: *Integrative Organismal Biology* 2.1, obaa001.

Crandell, K and Tobalske B (2015). “Kinematics and aerodynamics of avian upstrokes during slow flight”. In: *The Journal of experimental biology* 218.16, pp. 2518–2527.

Geyer, T, Sarradj E, and Fritzsche C (2013). “Silent owl flight: comparative acoustic wind tunnel measurements on prepared wings”. In: *Acta Acustica United with Acustica* 99.1, pp. 139–153.

Geyer, T, Sarradj E, and Fritzsche C (2014). “Measuring owl flight noise”. In: *INTER-NOISE and NOISE-CON Congress and Conference Proceedings*. Vol. 249. 8. Institute of Noise Control Engineering, pp. 183–198.

Geyer, T, Wasala S, Cater J, Norris S, and Sarradj E (2016a). “Experimental investigation of leading edge hook structures for wind turbine noise reduction”. In: *22nd AIAA/CEAS Aeroacoustics Conference*, p. 2954.

Geyer, T, Claus V, and Sarradj E (2016b). “Silent owl flight: The effect of the leading edge comb on the gliding flight noise”. In: *22nd AIAA/CEAS Aeroacoustics Conference*, p. 3017.

Geyer, T, Claus V, Hall P, and Sarradj E (2017). “Silent owl flight: the effect of the leading edge comb”. In: *International Journal of Aeroacoustics* 16.3, pp. 115–134.

Gharali, K, Tam N, and Johnson D (2014). “A PIV load and flow structure study of a serrated dynamic airfoil”. In: *Lisbon 17th Int. Symp. On Applications of Laser Techniques to Fluid Mechanics, Lisbon, Portugal*, pp. 1–8.

Graham, RR (1934). “The silent flight of owls”. In: *The Aeronautical Journal* 38.286, pp. 837–843.

Hansen, K, Kelso R, and Doolan C (2012). “Reduction of flow induced airfoil tonal noise using leading edge sinusoidal modifications”. In: *Acoustics Australia* 40.3, pp. 172–177.

Hausmann, L, Plachta D, Singheiser M, Brill S, and Wagner H (2008). “In-flight corrections in free-flying barn owls (Tyto alba) during sound localization tasks”. In: *Journal of Experimental Biology* 211.18, pp. 2976–2988.

Hedenström, A, Rosén M, and Spedding G (2006). “Vortex wakes generated by robins Erithacus rubecula during free flight in a wind tunnel”. In: *Journal of the Royal Society Interface* 3.7, pp. 263–276.

Hersh, A, Soderman P, and Hayden R (1974). “Investigation of acoustic effects of leading-edge serrations on airfoils”. In: *Journal of Aircraft* 11.4, pp. 197–202.

Ito, S (2009). “Aerodynamic influence of leading-edge serrations on an airfoil in a low Reynolds number-A study of an owl wing with leading edge serrations”. In: *Journal of Biomechanical Science and Engineering* 4.1, pp. 117–123.

Jaworski, W and N Peake (2020). “Aeroacoustics of silent owl flight”. In: *Annual Review of Fluid Mechanics* 52, pp. 395–420.

Klän, S, Klaas M, and Schröder W (2010). “The influence of leading edge serrations on the flow field of an artificial owl wing”. In: *28th AIAA Applied Aerodynamics Conference*, p. 4942.

Konishi, M (1973). “How the owl tracks its prey: experiments with trained barn owls reveal how their acute sense of hearing enables them to catch prey in the dark”. In: *American Scientist* 61.4, pp. 414–424.

Kroeger, R, Gruschka H, Helvey T, et al. (1972). *Low speed aerodynamics for ultra-quiet flight*. Air Force Flight Dynamics Laboratory, Air Force Systems Command, United States Air Force.

Lentink, D, Van Heijst G, Muijres F, and Van Leeuwen J (2010). “Vortex interactions with flapping wings and fins can be unpredictable”. In: *Biology Letters* 6.3, pp. 394–397.

Lilley, G (1998). “A study of the silent flight of the owl”. In: *4th AIAA/CEAS aeroacoustics conference*, p. 2340.

Muijres, F, Bowlin M, Johansson C, and Hedenström A (2012). “Vortex wake, downwash distribution, aerodynamic performance and wingbeat kinematics in slow-flying pied flycatchers”. In: *Journal of the Royal Society Interface* 9.67, pp. 292–303.

Muthuramalingam, M, Puckert D, Rist U, and Bruecker C (2020a). “Transition delay using biomimetic fish scale arrays”. In: *Scientific Reports* 10.1, p. 14534.

Muthuramalingam, M, Talboys E, Wagner H, and Bruecker C (2020b). “Flow turning effect and laminar control by the 3D curvature of leading edge serrations from owl wing”. In: *Bioinspiration & Biomimetics* 16.2, p. 026010. DOI: 10.1088/1748-3190/abc6b4. URL: https://dx.doi.org/10.1088/1748-3190/abc6b4.

Narayanan, S, Chaitanya P, Haeri S, Joseph P, Kim J.W, and Polacsek C (2015). “Airfoil noise reductions through leading edge serrations”. In: *Physics of Fluids* 27.2.

Neuhaus, W, Bretting H, and Schweizer B (1973). “Morphologische und funktionelle Untersuchungen über den’lautlosen’Flug der Eulen (Strix aluco) im Vergleich zum Flug der Enten (Anas platyrhynchos)”. In: *Biologisches Zentralblatt* 92, pp. 495–512.

Norberg, U (1990). *Vertebrate flight: mechanics, physiology, morphology, ecology and evolution*. Vol. 27. Springer Science & Business Media.

Payne, R (1971). “Acoustic location of prey by barn owls (Tyto alba)”. In: *Journal of Experimental Biology* 54.3, pp. 535–573.

Raffel, M, Willert C, Scarano F, Kähler C, Wereley S, and Kompenhans J (2018). *Particle image velocimetry: a practical guide*. Springer.

Rao, C, Ikeda T, Nakata T, and Liu H (2017). “Owl-inspired leading-edge serrations play a crucial role in aerodynamic force production and sound suppression”. In: *Bioinspiration & biomimetics* 12.4, p. 046008.

Sarradj, E, Fritzsche C, and Geyer T (2011). “Silent owl flight: bird flyover noise measurements”. In: *AIAA journal* 49.4, pp. 769–779.

Saussaman, Tanner, Asif Nafi, David Charland, Hadar Ben-Gida, and Roi Gurka (2023). “The role of leading-edge serrations in controlling the flow over owls’ wing”. In: *Bioinspiration & biomimetics* 18.6, p. 066001.

Schwind, R and Allen H (1973). “The effects of leading-edge serrations on reducing flow unsteadiness about airfoils.” In: *Aerospace Sciences Meeting*. AIAA PAPER 73-89.

Sick, H (1937). “Morphologisch-funktionelle Untersuchungen über die Feinstruktur der Vogelfeder”. In: *Journal für Ornithologie* 85.2, pp. 206–372.

Thielicke, W and Stamhuis E.J (2014). “PIVlab Towards User-friendly, Affordable and Accurate Digital Particle Image Velocimetry in MATLAB.” In: *Journal of Open Research Software* 2(1):e30. DOI: http://dx.doi.org/10.5334/jors.bl.

Tobalske, B, J Hearn, and D Warrick (2009). “Aerodynamics of intermittent bounds in flying birds”. In: *Experiments in fluids* 46, pp. 963–973.

Townsend, AA (1947). “Measurements in the turbulent wake of a cylinder”. In: *Proceedings of the Royal Society of London. Series A. Mathematical and Physical Sciences* 190.1023, pp. 551–561.

Wagner, H, Weger M, Klaas M, and Schröder W (2017). “Features of owl wings that promote silent flight”. In: *Interface focus* 7.1, p. 20160078.

Weger, M and Wagner H (2016). “Morphological variations of leading-edge serrations in owls (Strigiformes)”. In: *PLoS One* 11.3, e0149236.

Williams, J and Hall L (1970). “Aerodynamic sound generation by turbulent flow in the vicinity of a scattering half plane”. In: *Journal of fluid mechanics* 40.4, pp. 657–670.

Williamson, C (1996). “Vortex dynamics in the cylinder wake”. In: *Annual review of fluid mechanics* 28.1, pp. 477–539.

Winzen, A, Roidl B, Klän S, Klaas M, and Schröder W (2014). “Particle-image velocimetry and force measurements of leading-edge serrations on owl-based wing models”. In: *Journal of Bionic Engineering* 11.3, pp. 423–438.

Zamponi, R, Satcunanathan S, Moreau S, Ragni D, Meinke M, Schröder W, and Schram C (2020). “On the role of turbulence distortion on leading-edge noise reduction by means of porosity”. In: *Journal of Sound and Vibration* 485, p. 115561.

Zierep, J (2013). *Ähnlichkeitsgesetze und Modellregeln der Strömungslehre*. Springer-Verlag.

Appendix

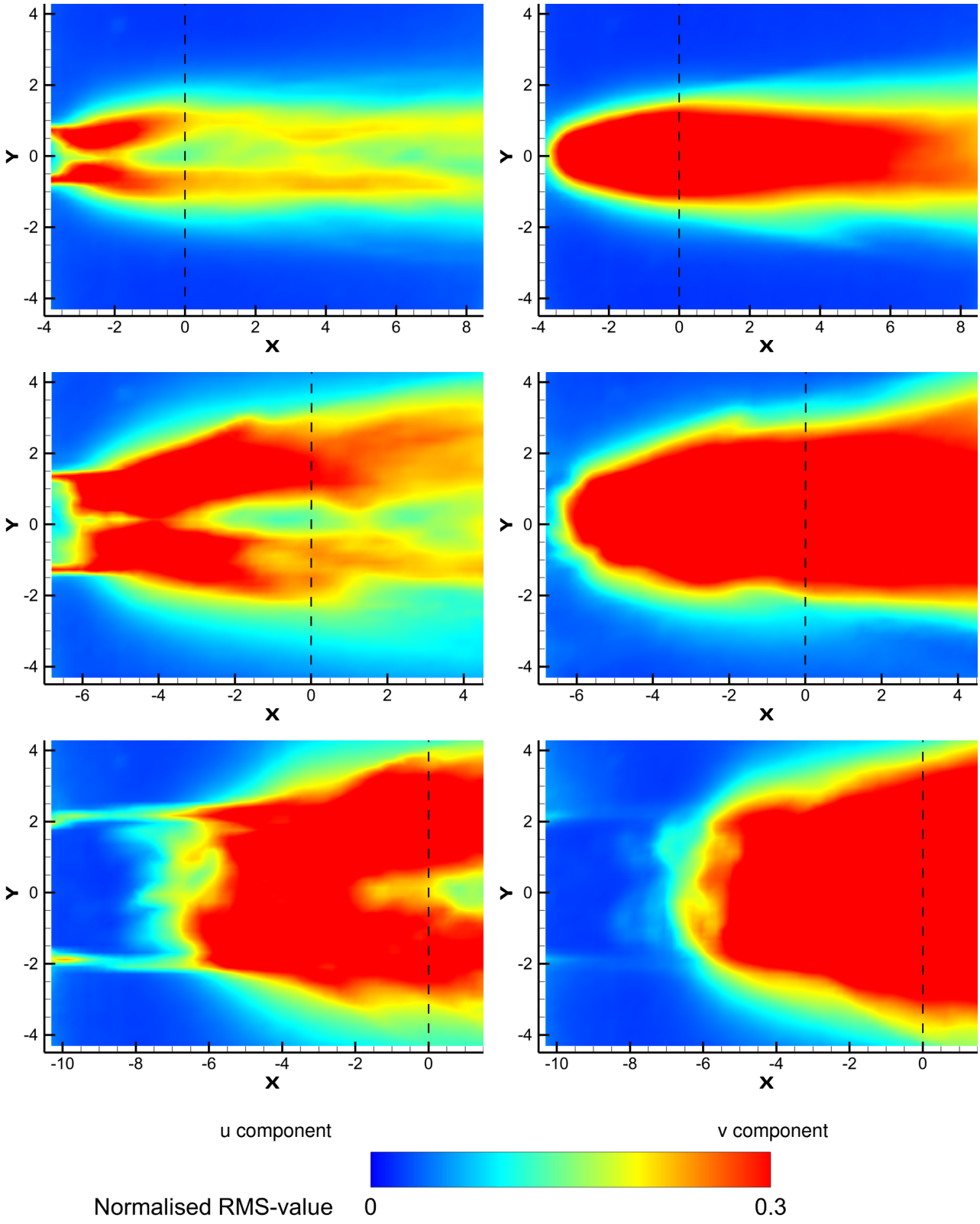

Figure 13: Contour plots of velocity fluctuation intensity in u-component (left column) and v-component (right column) in the wake of a D-shaped cylinder, shown in the frame of reference of the cylinder's aft. The dashed black line is where the tips of the barbs would be located. First row is $D/H = 1$, second row is $D/H = 2$ and the last row is $D/H = 3$.

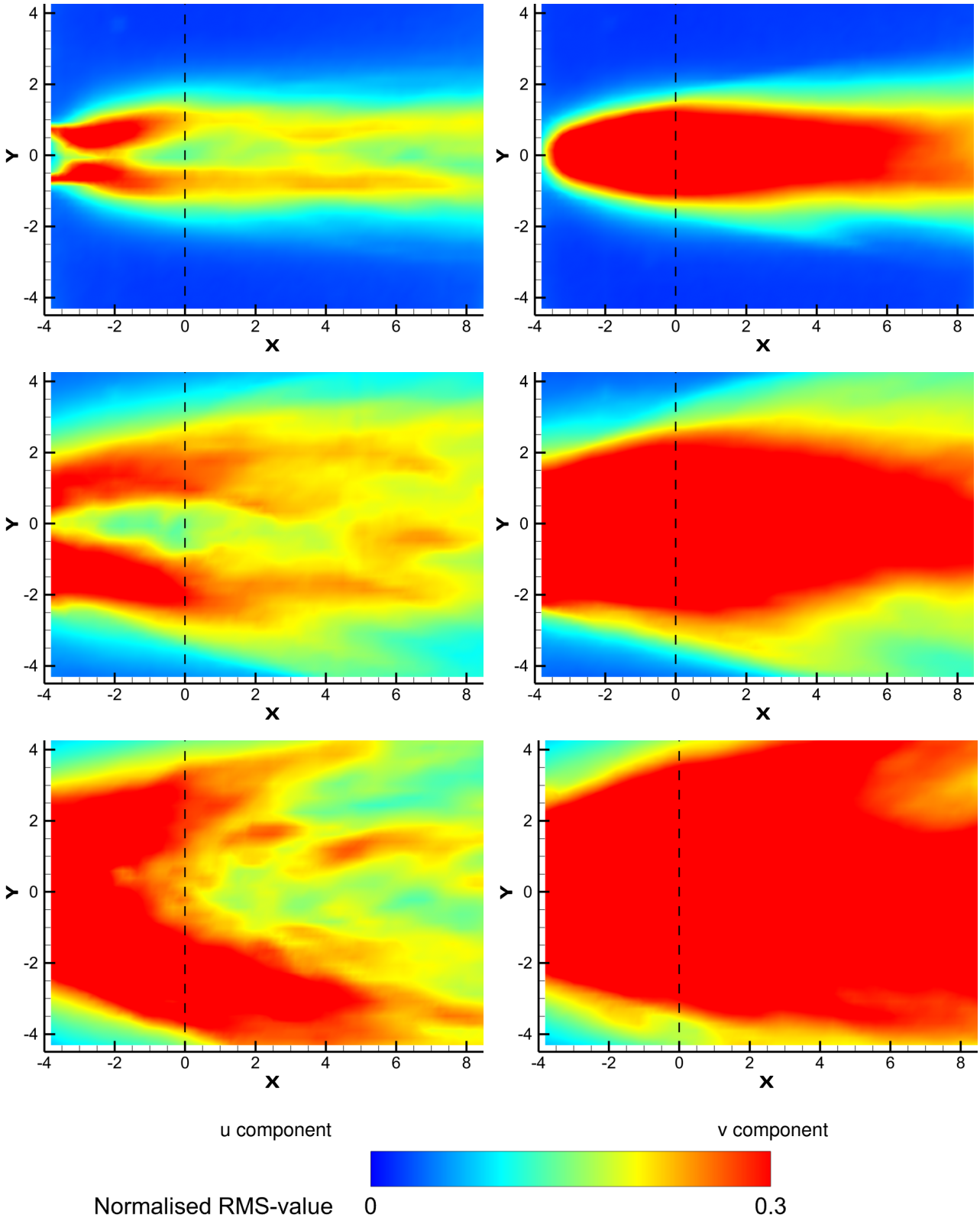

Figure 14: Same as in fig. 13 but shown in the frame of reference of the serrations. The dashed black line is where the tips of the barbs would be located.

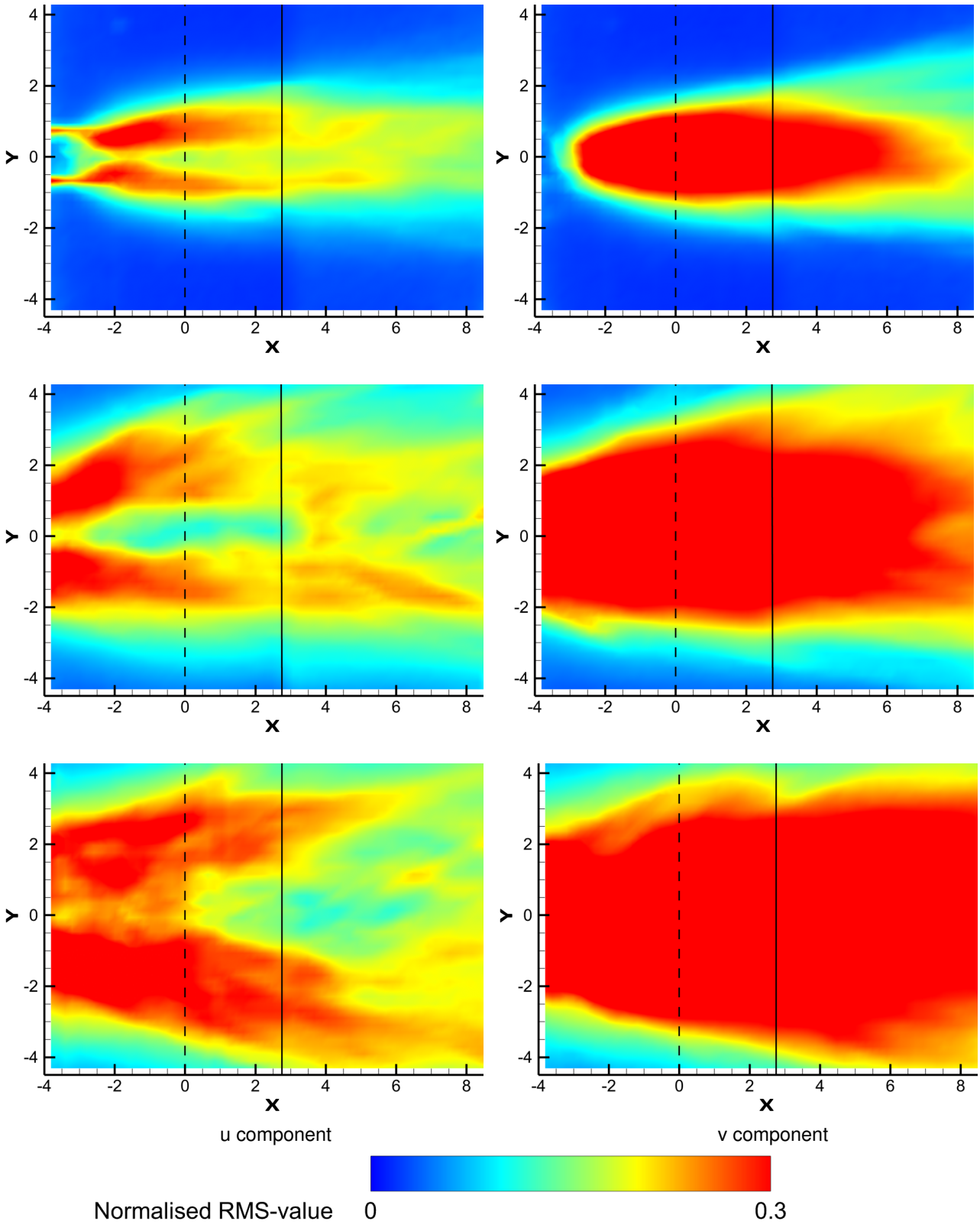

Figure 15: Same as in fig. 14 but shown for the case of the flat plate without serrations. The solid black line indicates the leading edge of the plate.

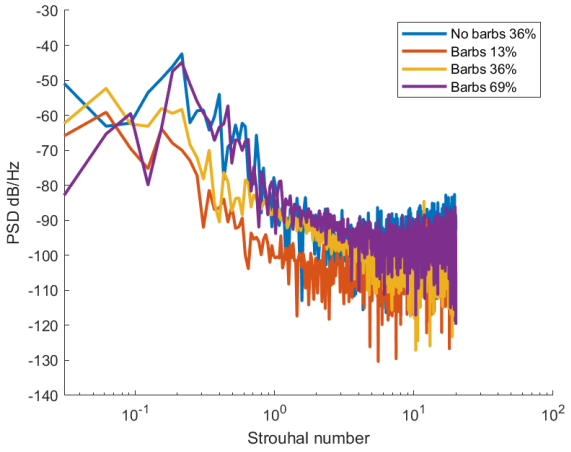

(a) $D/H = 1$

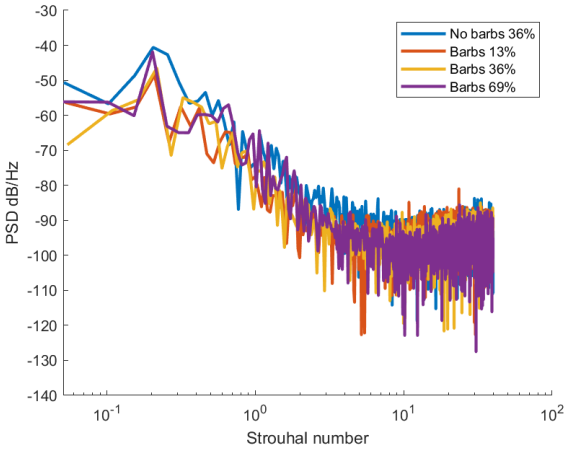

(b) $D/H = 2$

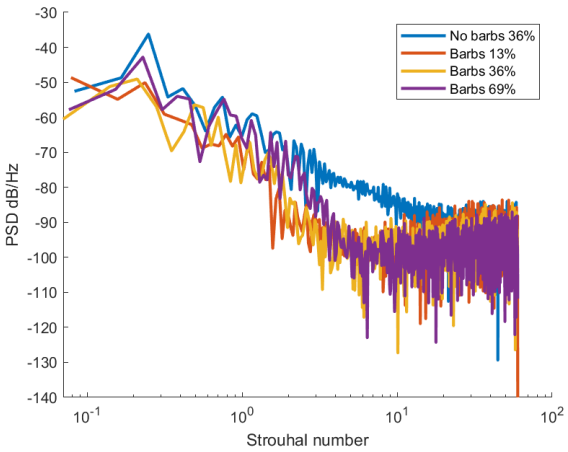

(c) $D/H = 3$

Figure 16: Power spectral density of v-velocity component of the fluctuations in the wake of each of the cylinders. Plate 36% is the plate in the cylinder wake without the barbs attached, used as the reference case. Barbs 13%, 36% and 69% are the frequencies found downstream of the barbs at each respective height tested.